SCIENCE CHINA
Technological Sciences

•Article•

July 2024 Vol.67 No.7: 2244–2254
https://doi.org/10.1007/s11431-023-2612-3

Exciting broadband thermochromic transmission property opposite to vanadium dioxide in the atmospheric window

GONG YiQuan, GUO YanMing*, CHEN ShuNi, LI Meng, PAN QingHui & SHUAI Yong

Ministry of Industry and Information Technology Key Laboratory of Aerospace Thermophysics, School of Energy Science and Engineering, Harbin Institute of Technology, Harbin 150001, China

Received October 14, 2023; accepted January 31, 2024; published online July 1, 2024

The traditional telecommunications band performs poorly in harsh weather conditions due to atmospheric absorption. In recent years, researchers have begun to study optical communication through atmospheric windows, and optical switches are an essential component of optical communication. A broadband atmospheric window optical switch was proposed based on Vanadium dioxide and magnetic polaritons (MP). It is formed by the stacking of two metal-dielectric-metal structures. The simulation results show that the modulation depth can reach 98.38%, and the extinction ratio is 17.93 dB. By calculating the magnetic field, we confirmed that the reason for the "off" mode is the coupling between the different MP modes, while the "on" mode is the excitation of MP. The optical switch we proposed may be applied to radiation cooling and optical satellite communication.

optical communication, thermochromic property, atmospheric window, optical switch, magnetic polariton

Citation: Gong Y Q, Guo Y M, Chen S N, et al. Exciting broadband thermochromic transmission property opposite to vanadium dioxide in the atmospheric window. Sci China Tech Sci, 2024, 67: 2244–2254, https://doi.org/10.1007/s11431-023-2612-3

1 Introduction

Due to the continuous development of optical communication technology, the traditional telecommunications bands (1260 to 1625 nm) are no longer sufficient to meet current needs, particularly for optical satellite communication [1]. The primary reason for this is that traditional bands can lead to significant energy losses in atmospheric environments characterized by fog and adverse conditions. This is due to the strong absorption of water molecules at 1450 nm, which is caused by the resonance of hydrogen and oxygen [2]. Consequently, there has been a surge in the investigation of optical communication in the atmospheric band [3]. Recent research has shown that optical communication through atmospheric windows still performs well under extreme weather conditions [4]. Optical switches are one of the most essential components in optical communication. Nanomaterials have been widely used in the field of optical switches due to their unique optical, electrical, and magnetic properties [5–9]. Optical switches are mainly achieved by magnetic polaritons (MP) [10], surface plasmon polaritons [11], Fabry-Perot resonance [12–15], and localized surface plasmon resonance [16]. Implementing optical switching modes relies on heat [17] and electricity [18,19]. Electrically driven optical switches mainly rely on electrochromic materials, such as tungsten trioxide and molybdenum trioxide [20], while thermally driven optical switches mainly rely on phase change materials. Vanadium dioxide (VO_2) is the most popular phase change material due to its phase change temperature near room temperature (68°C) [21], while other materials, such as $Ge_2Sb_2Te_5$ (GST), have a phase change temperature of 160°C [22]. In addition, the phase transition time of VO_2 is only 60 ns [23], which is one order of magnitude faster than traditional mechanical and acoustic

*Corresponding author (email: guoyanming@hit.edu.cn)

switches, making it the preferred material for thermal-driven optical switches. When the temperature is above 68°C, the VO_2 exhibits metallic properties, while at a temperature below 68°C, it exhibits insulation [24]. What is even more exciting is that in recent years, researchers have demonstrated a tunable phase transition temperature of VO_2 from 40°C to 75°C by doping elements such as W [25], Mo [26], and Zr [27], which undoubtedly increases the applicability of VO_2.

There have been many international studies on infrared optical switches and modulators based on indium tin oxide (ITO) [28], VO_2 [29–32], GST [33], and graphene [34]. For example, in terms of narrowband optical switches, Guo et al. [10] designed a periodic Ag-VO_2-Ag slit array structure at a wavelength of 2.53 μm based on MP, and the extinction ratio (ER) of the optical is 12.4 dB. Moreover, Wang et al. [11] proposed a two-dimensional cylindrical column structure at a wavelength of 4.3 μm, and the ER reaches up to 22.14 dB. Researchers have also designed many broadband optical switches with different mechanisms. Figure 1 compares the spectral average ER and bandwidth of optical switches and modulators reported by several groups. Dalal and Sharma [29] used multiple gold disks with different radii to excite plasma polaritons, resulting in a bandwidth of 650 nm and an ER of 5 dB. Xie et al. [28] designed a three-dimensional cross-structure based on ITO. They combined epsilon-near-zero (ENZ) with plasmon resonance for the first time and successfully achieved a transmission optical switch with an ER of 17 dB and a bandwidth of 300 nm. Markov et al. [30] combined gold nanodisks with VO_2 thin films on silicon dioxide to achieve near-field plasma coupling, and their proposed optical switch achieves a bandwidth of 100 nm and an ER of 8.9 dB. What's more, Thomas et al. [31] placed an Au nanowire array on a VO_2 thin film to excite plasma polaritons, achieving a bandwidth of 800 nm and an ER of 4 dB. Researchers have made significant breakthroughs in the narrowband optical switch of infrared. However, the broadband optical switch cannot simultaneously obtain wide bandwidth and high ER. And there are no reported transmission optical switches for atmospheric windows. Therefore, studying a transmission optical switch with broadband, high ER, and working wavelength in the atmospheric window is necessary [35–38].

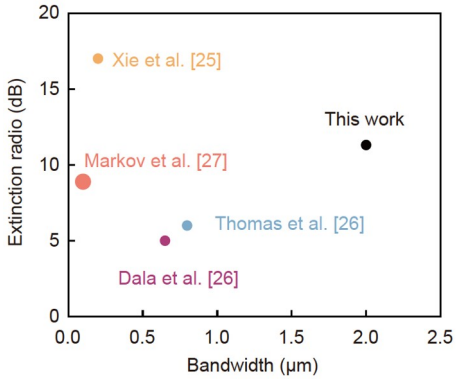

Figure 1 (Color online) Comparison of modulation performances between this work and previous studies.

In this paper, we proposed a broadband optical switch whose working wavelength is in the atmospheric window, achieved by stacking two MDM structures. When VO_2 is in the metallic state, the switch is in the "on" mode, while when VO_2 is insulating, the switch is in the "off" mode. To facilitate readers to adjust the working wavelength, we have provided the design steps for this optical switch. The simulation results of the time-domain difference method (FDTD) indicate that the maximum ER of our proposed broadband optical switch is 17.93 dB, and the maximum modulation depth (MD) is 98.83%. Subsequently, we conducted a mechanism analysis, and the magnetic field distribution showed that the "on" mode was due to the excitation of the MP, while the "off" mode was due to the coupling of the MP. The oblique incidence simulation shows that our proposed optical switch can maintain an ER of above 8 dB and an MD of 80% under high-angle incidence. The final robust analysis results indicate that our proposed broadband optical switch performs well despite machining errors. Moreover, due to the excitation and coupling of MP applied to MDM structures, phase change materials can be transformed into electrochromic materials to design electrically driven optical switches.

2 Modelling and numerical method

Figure 2(a) depicts the proposed atmospheric window broadband optical switch. This periodic structure consists of a seven-layer metal-dielectric interlaced structure. Four gold (Au) slit array layers with thickness h = 850 nm were separated by three VO_2 slit array spacers with distances d_1 = 110 nm and d_2 = 25 nm. The period of the slit array is Λ = 580 nm, the width w = 400 nm, and the intermediate dielectric thickness b = 180 nm. A transverse magnetic (TM) plane wave with wavelength λ and incidence angle θ was irradiated on the broadband wavelength selective optical switch.

The commercial package Lumerical FDTD Solutions was used to calculate electromagnetic fields and obtain spectral directional transmittance. To quantify the efficacy of the broadband wavelength optical switch, the defined wavelength-dependent MD and ER as [39]

$$\mathrm{MD}(\lambda)=\frac{\tau_{\mathrm{on}}(\lambda)-\tau_{\mathrm{off}}(\lambda)}{\tau_{\mathrm{on}}(\lambda)}, \tag{1}$$

$$\mathrm{ER}(\lambda)=10\lg\frac{\tau_{\mathrm{on}}(\lambda)}{\tau_{\mathrm{off}}(\lambda)}. \tag{2}$$

The frequency-dependent complex permittivity of Au is

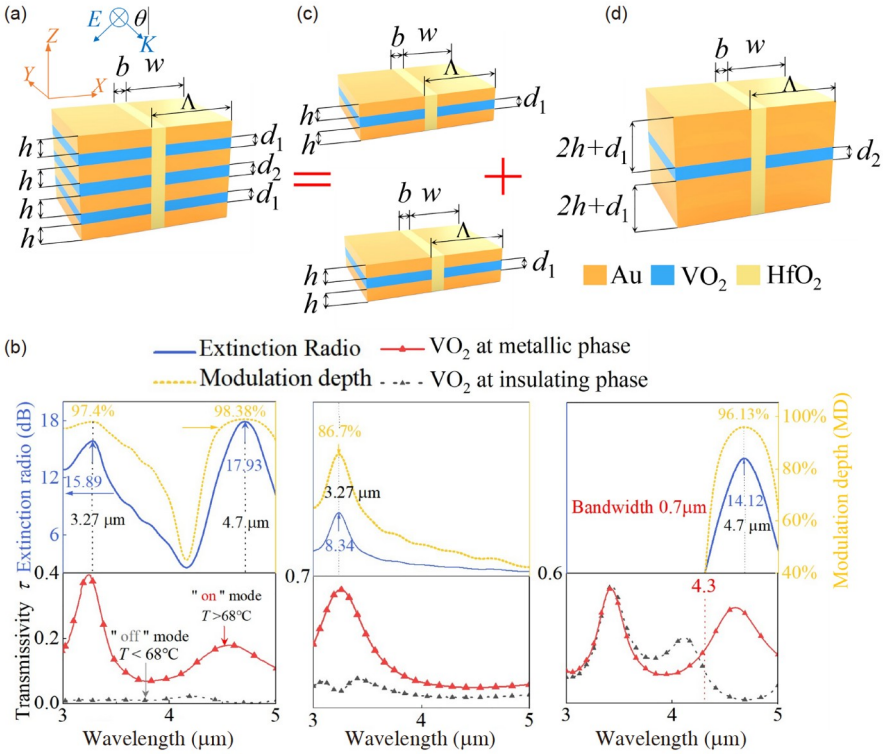

Figure 2 (Color online) (a) Schematic of the proposed atmospheric window broadband optical switch; (b) the spectral ER, MD, and spectral transmittance τ for the "on" and "off" modes of the proposed optical switch at normal incidence for TM waves; (c), (d) schematics of the broadband optical switch can be considered as the sum of two MDM structures. Spectral ER and MD are located below each structure, respectively.

obtained from the Palik Optical Handbook. The complex permittivity of metallic VO_2 is obtained from the Drude model [21]:

$$\varepsilon(\omega) = -\frac{\varepsilon_\infty \omega_p^2}{\omega^2 - i\gamma\omega}, \tag{3}$$

where the high-frequency constant $\varepsilon_\infty = 9$, plasma frequency $\omega_p = 8000\ \mathrm{cm}^{-1}$, and scattering frequency $\gamma = 10000\ \mathrm{cm}^{-1}$. Although the dielectric constant of VO_2 is anisotropic when it is insulating, it can be approximately considered isotropic for the mid-infrared and can be described using the Lorentz model:

$$\varepsilon_i = \varepsilon_\infty + \sum_{j=1}^{N} \frac{S_j \omega_j^2}{\omega_j^2 - i\omega\gamma_j - \omega^2}, \tag{4}$$

where S_j is the oscillator strength, ω_j is the phonon vibration frequency, and γ_j is the scattering rate. S_j, ω_j, and γ_j are shown in Table 1.

Because the imaginary part of the complex permittivity is almost zero for HfO_2 ($\varepsilon''(\lambda)$=0), the real part is described with a Sellmeier model [40]:

$$\varepsilon'(\lambda) = \frac{A_s \lambda^2 \lambda_0^2}{\lambda^2 - \lambda_0^2}, \tag{5}$$

where $A_s = 1.59\times10^{-2}\ \mathrm{nm}^{-2}$ and $\lambda_0 = 10.16$ nm are the adjustable parameters in the Sellmeier model.

Owing to the wireless extension of the switch in the y-axis, only the xz-plane needs to be calculated. For normal incidence, perfectly matched layers are applied in the z-direction, and the periodic boundary condition is set in the x-direction. However, the Bloch boundary condition is applied in the x-direction for oblique incidence cases. For oblique incidence, we used BRAST light sources, and for normal incidence, we used periodic plane waves. To ensure the accuracy of the calculation, a mesh with a step size of 1 nm is applied in the x- and z-directions, and the numerical convergence criteria were less than 10^{-6}. The collected wavelength was 3–5 μm with 1000 wavelength points.

Figure 2(b) depicts the ER, MD, and spectral transmittance for the "on" and "off" modes of our proposed optical switch at normal incidence for TM incidence in the atmospheric window. The ER can reach 17.93 dB, while the MD can reach 98.38%. Two peaks are located at wavelengths 3.27 and 4.7 μm, respectively. This is because a periodic triple-layer MDM structure based on VO_2 can be used as an optical switch for a specific wavelength, and our proposed structure can be regarded as the sum of two MDM structures, as shown in Figure 2(c) and (d). In addition, we can conclude that for Structure 2, our stacking enhances its effectiveness, increasing its ER from 8.34 to 15.89 dB, while for Structure 3, stacking increases its bandwidth from 0.7 to 2 μm.

We start with Structure 2 in Figure 2(c) to obtain our proposed optical switch. Select period Λ = 580 nm, and the

Table 1 Lorentz oscillator model parameters of insulating VO_2

No.	S_j	ω_j	γ_j
1	0.54	189	0.012
2	13.0	270	0.07
3	7	310	0.05
4	0.7	340	0.024
5	3.1	505	0.07
6	4.8	600	0.074
7	0.15	710	0.06
8	1.3	10000	0.4
		ε_∞=10	

thickness of the first layer of VO_2 d_1= 110 nm so that the working wavelength is in the atmospheric window. Figure 3(a) and (b) plot the spectral τ as a function of wavelength and varying the Au layer height h when the VO_2 is in the metallic and insulating phase, respectively. Note that MP_V2 (second-order MP excited in the vertical direction) is for Structure 2 instead of Structure 1. Figure 3(a) and (b) show the $MP_H^{1,3}1$ and MP_V2 coupling when the Au slit height is 800 nm and the coupling wavelength is 3.27 μm. After confirming the Au slit height h, we start calculating the proposed model, as shown in Structure 1 in Figure 2(a). Figure 3(c) and (d) present the contour plot of the spectral τ as a function of wavelength and varying the VO_2 slit height d_2 when the VO_2 is in the metallic and insulating phase, respectively, at fixed geometric parameters. Figure 3(d) shows that $MP_H^2 1$ (the first-order MP excited in the horizontal direction for the second layer of VO_2) coupled with MP_V3 when the VO_2 slit height d_2 was 25 nm, and the coupling wavelength was 4.7 μm, and this is why there are two peaks in Figure 2(b).

3 Results and discussion

3.1 Mechanism analysis

In terms of VO_2 in the metallic phase for the "on" mode, the magnetic field is strongly localized at the slit, and primary resonance occurs, as shown in Figure 4(a) and (b). Therefore, the ER peaks at 3.27 and 4.7 μm can be attributed to the resonance of MP_V4 and MP_V3, respectively.

The equivalent inductor-capacitor (LC) circuit model confirms that MP_V4 and MP_V3 are excited in Structure 1 [41–43]. The HfO_2 between the Au strips is considered as dielectric capacitance C, and Au sidewalls are considered to

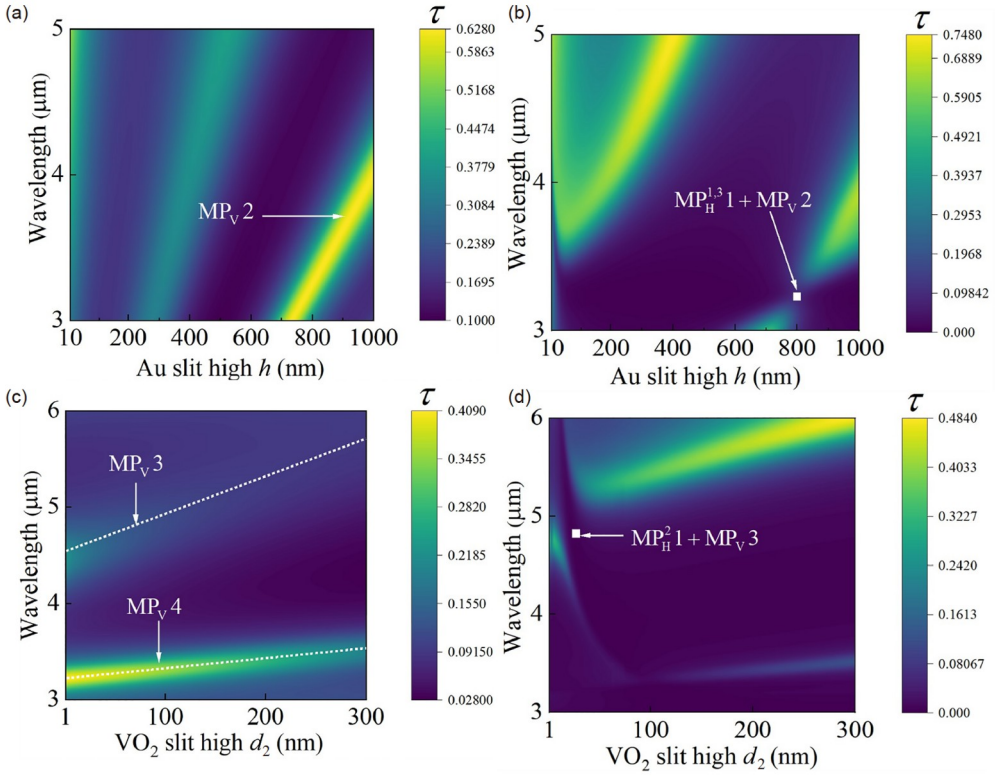

Figure 3 (Color online) (a) Contour plot of spectral τ as a function of wavelength and varying Au slit height h for Structure 2 when the VO_2 is in metallic phase; (b) contour plot of spectral τ as a function of wavelength and varying Au slit height h for Structure 2 when the VO_2 is in an insulating phase; (c) contour plot of spectral as a function of wavelength and varying VO_2 slit height d_2 for Structure 1 when the VO_2 is in metallic phase; the dashed line represents the relationship between resonance wavelength and d_2 obtained from the equivalent circuit model (to be discussed later); (d) contour plot of spectral τ as a function of wavelength and varying VO_2 slit height d_2 for Structure 1 when the VO_2 is in the insulating phase.

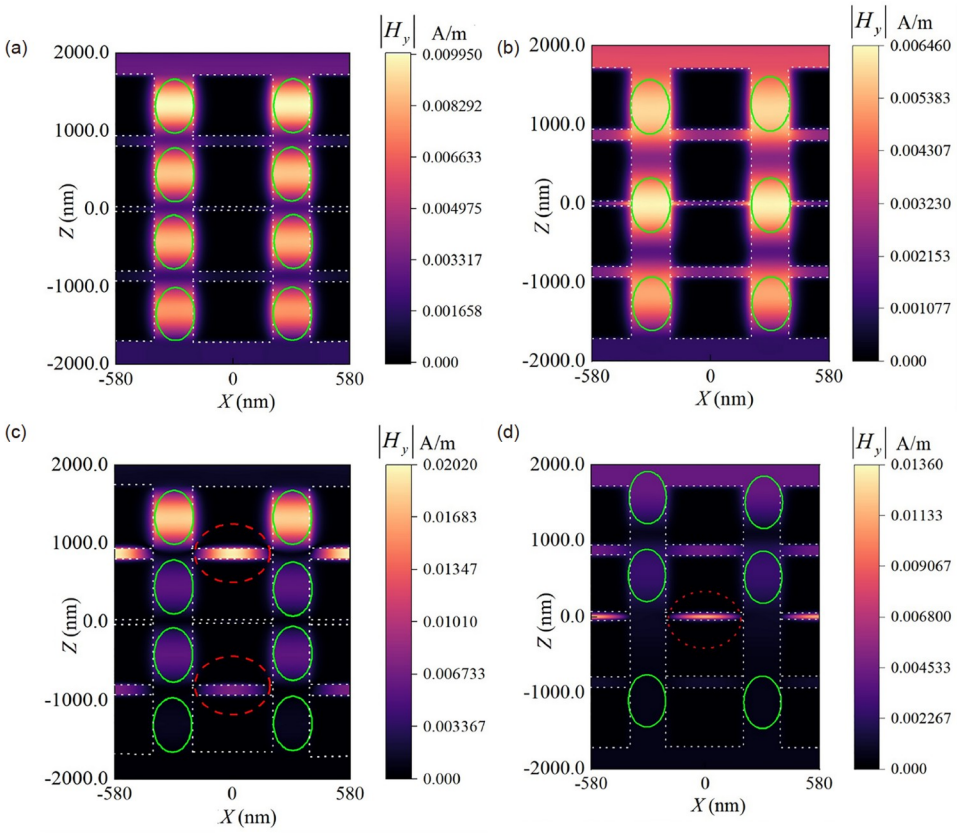

Figure 4 (Color online) Normal incidence. (a), (b) Magnetic field distributions at resonant wavelength 3.27 and 4.7 μm, respectively, when the optical switch is in "on" mode; (c), (d) magnetic field distributions at wavelength 3.27 and 4.7 μm, respectively, when the optical switch is in "off" mode. The dashed circle represents the resonant circuit of the *xy*-plane, whereas the solid circle represents the resonant circuit of the *xz*-plane.

be inductance L. The capacitance of intermediate HfO_2 can be expressed as

$$C = c_1 \frac{\varepsilon_d \varepsilon_0 h_i l}{b}, \tag{6}$$

where ε_0 is the free-space permittivity, ε_d is the relative permittivity of HfO_2, l is the length of the y-axis and can be assumed to be 1. c_1 is the numerical factor accounting for the non-uniform charge distribution at the strip sidewall surfaces; here, $c_1 = 0.24$. is equal to $H/4$ and $H/3$ for MP_V4 and MP_V3, respectively, where H is the total height of Structure 1.

The inductance L is equal to the sum of the inductances of the two parallel strips and the dynamic inductance, which can be written as

$$L = \frac{0.5\mu_0 h_i b}{l} - \frac{h_i}{\varepsilon_0 \omega^2 l \delta} \frac{\varepsilon'}{\varepsilon'^2 + \varepsilon''^2}. \tag{7}$$

For materials that can be described using the Drude model, the inductance can be expressed as

$$L = \frac{0.5\mu_0 h b}{l} - \frac{h_i}{\varepsilon_0 \omega_p^2 l \delta}. \tag{8}$$

where μ_0 is the permeability of vacuum, ε' and ε'' are the real and imaginary parts of the complex permittivity of Au, respectively, and δ is the power penetration depth, which can be written as

$$\delta = \frac{\lambda}{4\pi\kappa}, \tag{9}$$

where the extinction coefficient κ can be calculated from the complex dielectric. The resonant wavelength can be obtained as

$$\lambda_{MP} = c_0 2\pi\sqrt{LC}, \tag{10}$$

where c_0 is the speed of light in a vacuum, the resonance wavelength can be obtained from eqs. (6)–(10). The relationship between the resonance wavelength and d_2 is represented by the dashed line in Figure 3(c). It can be concluded that the ER peak at 3.27 and 4.7 μm can be attributed to the resonance of MP_V4 and MP_V3, respectively.

Regarding VO_2 at the insulating phase for the "off" mode, the mechanism of the "off" mode can be explained by coupling the MP modes. The electromagnetic field distributions at the MP resonant wavelength can describe the mechanism of MP coupling. The electromagnetic field distributions of the MP coupling at wavelength 3.27 and 4.7 μm are shown in Figure 4(c) and (d), respectively. From the perspective of the equivalent inductor-capacitor (LC) circuit model, the coupling can be explained as an interaction between the horizontal resonant circuit (dashed circle in Figure 4(c) and (d)

in the *xy*-plane) and the vertical resonant circuit (solid circle in Figure 4(c) and (d) in the *xz*-plane) that reaches a new balance, leading to a lower current circuit almost disappearing [41].

In Figure 4(c), owing to the coupling between $MP_H^{1,3}1$ and MP_V4, the incident electromagnetic waves were limited to the upper part of the structure and prevented from propagating downward. Similarly, the ER peak at 4.7 can be attributed to the coupling between $MP_H^{2}1$ and MP_V3. What's more, we found that there are two modes of MP coupling, as shown in Figure 4(c), where the horizontal resonant circuit is located just below the vertical resonant circuit, and the other, as shown in Figure 4(d), where the horizontal resonant circuit is located at the center of the vertical resonant circuit. By comparing Figure 4(a) and (c), we can observe that for the first MP coupling mode (the horizontal resonant circuit is below the vertical resonant circuit), the vertical resonant circuit does not move. However, for the second MP coupling mode (the horizontal resonant circuit is situated in the center of the vertical resonant circuit), comparing Figure 4(b) and (d), we can observe that the vertical resonant circuit will move upwards at this time, which leads to an upward movement of energy, this indicates that these two MP coupling modes have different reflection characteristics. We calculated their directional reflectivity from −80° to 80° to further investigate the differences between these two coupling modes, as shown in Figure 5(a). It can be concluded that these two MP coupling modes have opposite reflection characteristics. The reflectivity of MP coupling at 3.27 μm

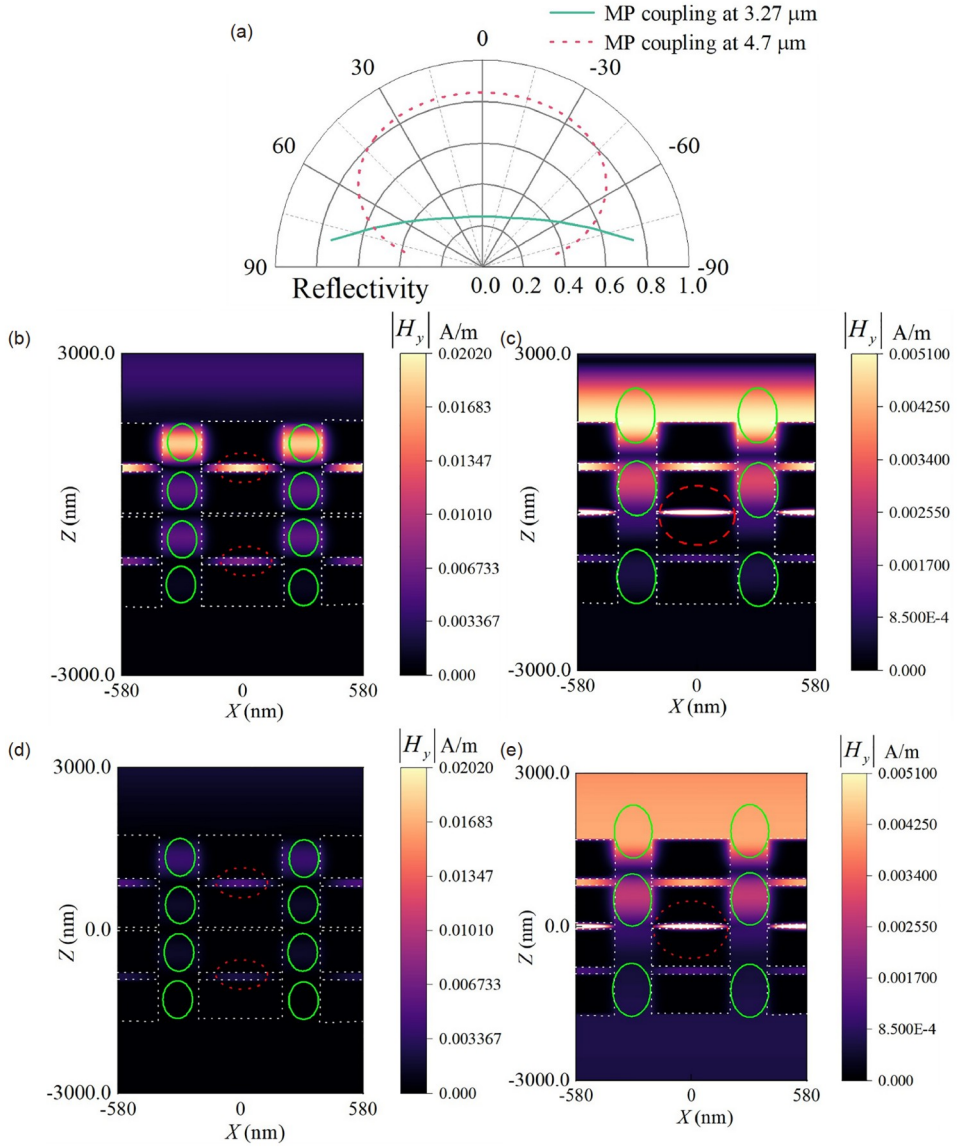

Figure 5 (Color online) (a) Directional reflectivity under different MP coupling modes; (b) magnetic field distribution with an incident angle of 30° at 3.27 μm; (c) magnetic field distribution with an incident angle of 30° at 4.7 μm; (d) magnetic field distribution with an incident angle of 80° at 3.27 μm; (e) magnetic field distribution with an incident angle of 80° at 4.7 μm.

increases with the increase of the incidence angle, while the reflectivity of MP coupling at 4.7 μm decreases with the increase of the incidence angle. The magnetic field distributions with incident angles of 30° and 80° at 3.27 μm are shown in Figure 5(b) and (d). The magnetic field distributions with incident angles of 30° and 80° at 4.7 μm are shown in Figure 5(c) and (e). For the convenience of comparison, we have unified the scale. From Figure 5(b) and (d), with the increase of incident angle, the magnetic field intensity of the second layer of VO_2 significantly decreases, leading to a decrease in absorption rate. At the same time, the transmittance remains unchanged, increasing reflectivity. However, the MP coupling situation at 4.7 μm is different. From Figure 5(c) and (d), it can be concluded that as the incident angle increases, the reflected magnetic field significantly weakens due to the coupling between the upward-moving magnetizing polaritons and the reflected waves. Moreover, as shown in Figure 5(b)–(e), MP coupling can also occur at high angles of incidence, indicating that our proposed optical switch can maintain good performance even at high angles of incidence. Because the MP coupling at 4.7 μm will cause the resonant circuit to rise, the actual height of the structure will be increased, which leads to MP_V3 is not excited at a specific frequency, so the coupling between MP_V3 and $MP_H^2 1$ is a broadband phenomenon, as shown in Figure 3(d). However, the MP coupling at 3.27 μm does not move the resonant circuit upward, so the excitation frequency of MPv4 is a fixed value, so the coupling of $MP_H^{1,3}1$ and MP_V4 is a narrowband phenomenon, as shown in Figure 3(b). Therefore, we must carefully select the height of the gold slit h to make $MP_H^{1,3}1$ and MP_V4 and the thickness of the second layer of VO_2 when MP_V3 and $MP_H^2 1$ coupling has an extensive selection range. Meanwhile, it also indicates that the MD peak at 4.7 μm has better robustness than that at 3.27 μm in the actual processing process (discussed in Section 3.3).

3.2 Oblique incidence analysis

The directional ER at different angles is also an important indicator for optical switches. Therefore, the directional ER from −80° to 80° at a wavelength of 3.27 and 4.7 μm is calculated as shown in Figure 6(a) and (b), respectively. As shown in Figure 5(a), the directional ER does not change with the incident angle because the resonant circuit in the *xy* plane (dashed circle in Figure 4(c)) is located just below the resonant circuit in the *xz*-plane (solid circle in Figure 4(c)), resulting in almost no change in transmittance with direction, thus ER does not change with direction, which is consistent with the conclusion of the previous research [10,44–46]. However, the situation is different when the wavelength is 4.7 μm, as the resonant circuit in the *xy* plane is in the center of the resonant circuit in the *xz*-plane, which causes the resonant circuit in the *xz*-plane to move upwards (compare Figure 4(b) and (d)), resulting in a change in reflectivity with incident angle (Figure 5(a)).

Therefore, the transmittance increases with the increase of the incident angle, which leads to a decrease in the direction MD at 4.7 μm. Figure 6(c) and (d) show the direction MD and ER of spectral average, respectively. It can be concluded that when the incident angle is 60, an ER of over 8 dB and an MD of over 80% can still be maintained. Therefore, our proposed optical switch still performs well under high-angle

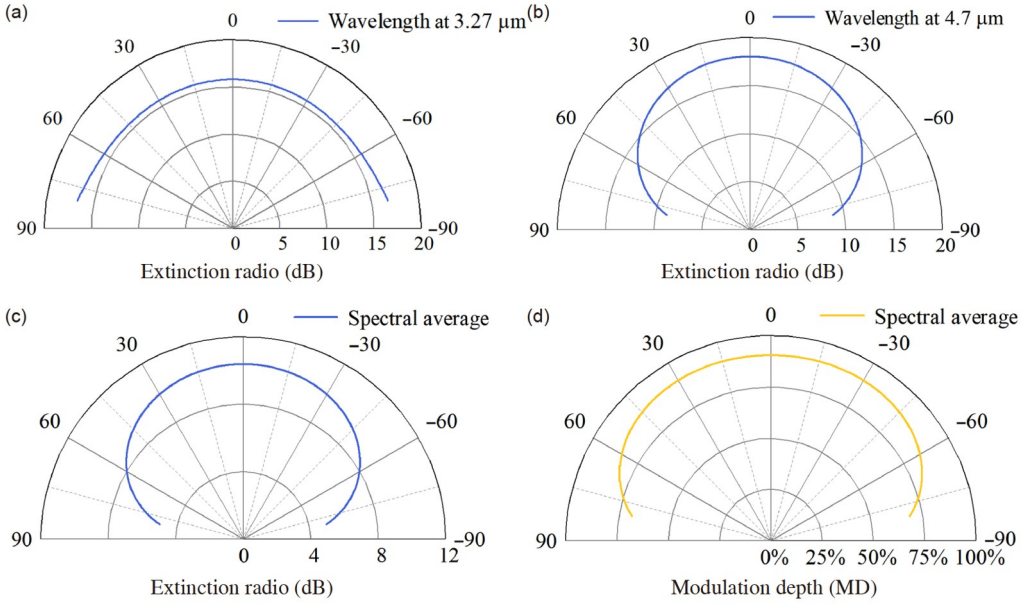

Figure 6 (Color online) Broadband atmospheric window optical switch directional ER at the wavelength (a) 3.27 μm, (b) 4.7 μm; (c) broadband atmospheric window optical switch directional spectral average ER; (d) broadband atmospheric window optical switch directional spectral average MD.

incidence conditions, which is consistent with the conclusion obtained from the magnetic field distribution in Figure 5(b)–(e).

3.3 Robustness analysis

Considering the uncertainty in the actual processing process, we assume that the random variables follow a Gaussian distribution with a variance of 5% of the design value [47]. However, using FDTD to calculate directly requires a significant amount of time. We begin by scanning the design parameters and exporting the data. We then utilize the intern installation package in Python for interpolation and ultimately generate a random number with a Gaussian distribution in Python for the statistical analysis of the results. The range, center value, variance, and scan interval of each design parameter are shown in Table 2, and the schematic diagram of each design parameter is shown in Figure 7(a).

Table 2 The range, center value, variance, and scan interval of each design parameter

Design parameters	Center value (nm)	Range (nm)	Variance (nm)	Scan interval (nm)
$h_1/h_2/h_3/h_4$	800	(720, 880)	40	1
w	400	(360, 440)	20	1
b	180	(162, 198)	9	1
d_1/d_3	110	(99, 121)	5.5	0.5
d_2	25	(22, 28)	1.25	0.25

The statistics are 100000, and due to the unknown probability density distribution that the results satisfy, the kernel smooth method in non-parametric estimation, a separation number of 0.1 is used.

Figure 7(b) depicts the probability density distributions at different h, and it can be concluded that the probability

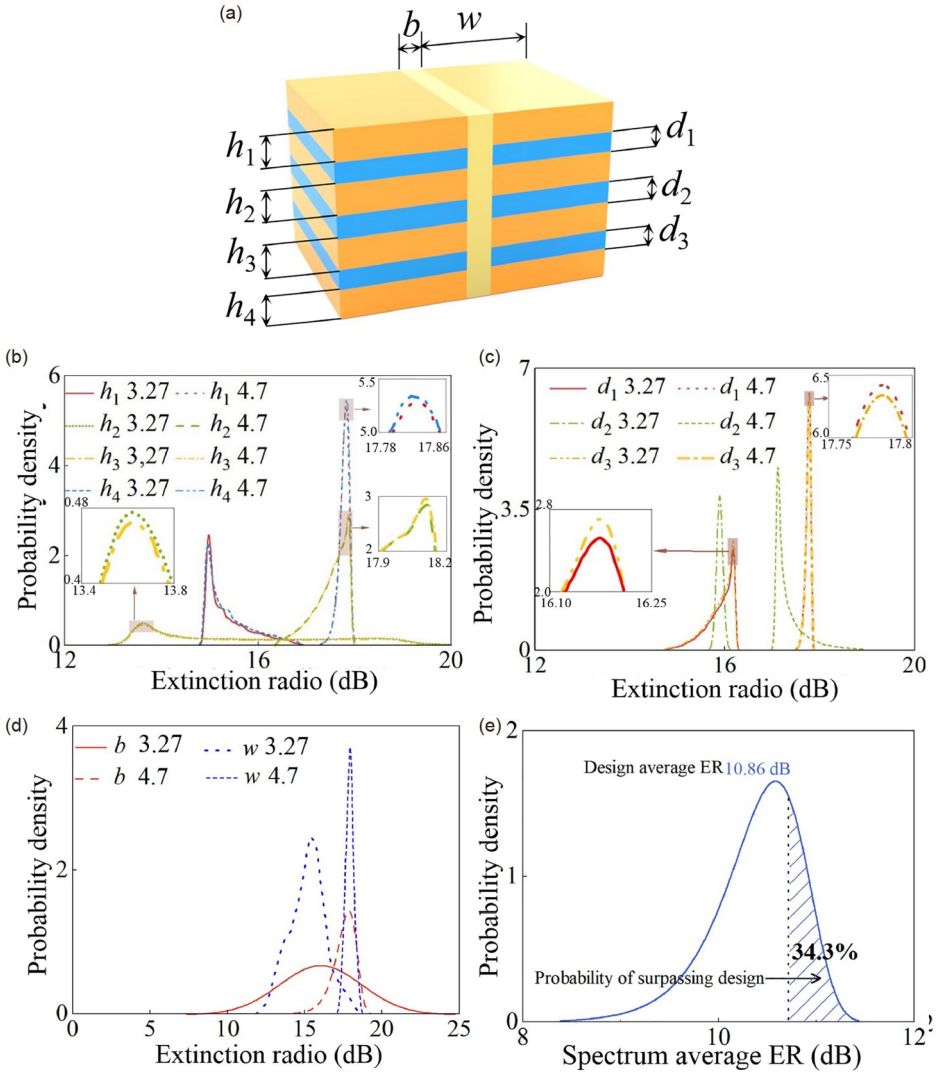

Figure 7 (Color online) (a) Schematic diagram of different variables; (b) probability density distributions of different h at 3.27 and 4.7 μm; (c) probability density distributions of VO_2 thickness in different layers at 3.27 and 4.7 μm; (d) probability density distributions of gold width w and central HfO_2 thickness b at 3.27 and 4.7 μm; (e) probability density of the spectrum average ER.

density distributions of h_1 and h_4 are the same, while the probability density distributions of h_2 and h_3 are the same, which is caused by the symmetry of the structure. Figure 7(c) depicts the probability density distributions at different VO_2 thicknesses. The reason why the probability density distributions of d_1 and d_3 are the same can be attributed to the symmetry of the structure. In addition, the probability density distribution of d_2 is narrowest at the wavelength of 3.27, indicating that d_2 has a smaller impact on the ER peak at 3.27. This is because the peak of ER at 3.27 μm is caused by the coupling between $MP_H^{1,3}1$ and MP_V4, which is independent of the thickness of the second layer of VO_2. Similarly, the probability density distributions of d_1 and d_3 can be attributed to the coupling between $MP_H^2 1$ and MP_V3. Figure 7(d) depicts the probability density distributions of the width of Au w and the gap b between HfO_2. The reason why the probability density distribution of w is narrowest is that the width of Au can only affect the numerical factor c_1 in the LC model, while the vast probability density of b is because the width of HfO_2 b directly affects the capacitance C and inductance L in the circuit model, as shown in eqs. (6) and (7), as a result, the excitation wavelength of MP is changed. Another point worth noting is that the probability density peak at 4.7 is narrow, so the MP coupling at 4.7 has good robustness [48], which is consistent with the conclusions drawn from the mechanism analysis. Figure 7(e) depicts the probability density of spectrum average ER. The designed spectrum average ER and MD are located near the maximum probability density, indicating that our design is easy to achieve in practical situations. In addition, for spectrum average ER and MD, there is a 34.3% probability that it is better than the design value. Therefore, the designed broadband optical switch has excellent robustness.

3.4 Application in harsh weather

Considering practical applications, we have defined the modulation depth of actual power (MDP), which is expressed as

$$\begin{aligned}\mathrm{MDP}(\lambda)&=\frac{p_{\mathrm{on}}-p_{\mathrm{off}}}{p_{\mathrm{out}}}\\&=\frac{p_{\mathrm{out}}\tau_{\mathrm{on}}\tau_a-p_{\mathrm{out}}\tau_{\mathrm{off}}\tau_a}{p_{\mathrm{out}}}\\&=(\tau_{\mathrm{on}}-\tau_{\mathrm{off}})\tau_a,\end{aligned}\tag{11}$$

where p_{out} represents the power of electromagnetic waves emitted from the ground into space, and p_{on} and p_{off} represent the electromagnetic wave power that the satellite can receive when the optical switch is in "on" and "off" modes, respectively. τ_0 is the atmospheric spectral transmittance under harsh weather conditions such as rainstorms and typhoons, which is calculated by subtracting the spectral absorption of dark clouds [49,50] from the 1976 US Standard default atmospheric transmittance [51]. Figure 8(a) and (b) represent contour maps of MDP under harsh weather conditions at traditional telecommunication bands (TTB) and atmospheric windows, respectively. It can be concluded that when $\tau_{\mathrm{on}}-\tau_{\mathrm{off}}$ is the same, the MDP of the atmospheric window is much greater than that of TTB, which further demonstrates the benefits of using atmospheric windows for optical satellite communication. The definition of $\mathrm{MDP}_{\mathrm{max}}$ at TTB is expressed as

$$\mathrm{MDP}_{\mathrm{max}}=\left(\int_{1.26}^{1.625}(\tau_{\mathrm{on}}-\tau_{\mathrm{off}})\tau_a\mathrm{d}\lambda\right)_{\mathrm{max}}=\int_{1.26}^{1.625}\tau_a\mathrm{d}\lambda.\tag{12}$$

It represents the MDP when = 1 and = 0, which means the best performance at TTB, as shown by the pink line in Figure 8(b). The white dotted line and yellow lines in Figure 8(b) represent the spectral MDP and average MPD of our proposed atmospheric window optical switch. Comparing the pink chain and white short chain line in Figure 8(b) in terms of spectral effect, our proposed optical switch outperforms $\mathrm{MDP}_{\mathrm{max}}$ in certain bands while comparing the yellow and pink lines in terms of average effect, the average effect of our proposed optical switch is better than the $\mathrm{MDP}_{\mathrm{max}}$ at TTB. In

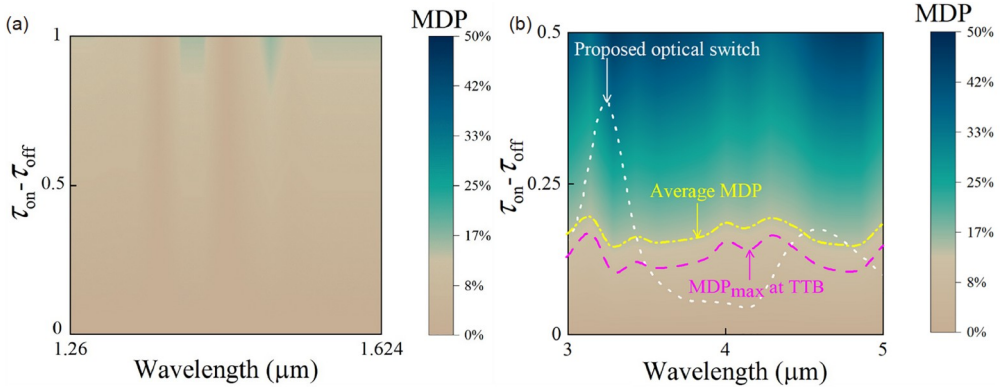

Figure 8 (Color online) (a) MDP under harsh weather conditions in TTB; (b) MDP under harsh weather conditions at atmospheric windows. The dotted line represents the variation of $\tau_{\mathrm{on}}-\tau_{\mathrm{off}}$ with wavelength of our proposed atmospheric window optical switch. The chain and short chain lines represent MDP's maximum values at TTB and average MDP, respectively.

general, the optical switch of the atmospheric window performs well under harsh weather conditions.

4 Conclusions

A broadband atmospheric window optical switch was proposed based on VO_2 and MP. The stacking of two MDM structures forms it. The simulation results show that the broadband wavelength optical switch has excellent performance, the maximum modulation depth (MD) can reach 98.38%, and the maximum extinction ratio (ER) is 17.93 dB. By calculating the magnetic field, we confirmed that the reason for the "off" mode is the coupling between the different MP modes, while the "on" mode is the excitation of MP. The oblique incidence simulation shows that our proposed optical switch can maintain an ER of above 8 dB and an MD of 80% under high-angle incidence. The robustness analysis shows that the broadband optical switch performs well despite machining errors. We compared the broadband infrared optical switches proposed by different scholars in recent years, and the results showed that our proposed optical switch maintained good ER characteristics while having a larger bandwidth. Finally, we calculated the comparison between TTB and atmospheric band MDP under adverse weather conditions, and the results showed that our proposed optical switch performed well under adverse weather conditions. In general, our proposed optical switch may be applied to radiation cooling and satellite communication.

This work was supported by the National Natural Science Foundation of China (Grant Nos. 52227813, 52106085), China Postdoctoral Science Foundation (Grant Nos. 2023M740905, 2021M690822), the Natural Science Foundation of Heilongjiang Province (Grant No. LH2023E043), the National Key Research and Development Program of China (Grant No. 2022YFE0210200), and the Fundamental Research Funds for the Central Universities (Grant No. 2022ZFJH04).

1 Chen B L, Chen Y J, Deng Z. Recent advances in high speed photodetectors for eSWIR/MWIR/LWIR applications. Photonics, 2021, 8: 1
2 Wang K, Wen W H, Wang Y X, et al. Order-of-magnitude multiphoton signal enhancement based on characterization of absorption spectra of immersion oils at the 1700-nm window. Opt Express, 2017, 25: 5909–5916
3 Flannigan L, Yoell L, Xu C Q. Mid-wave and long-wave infrared transmitters and detectors for optical satellite communications: A review. J Opt, 2022, 24: 043002
4 Biswal M R, Arya S, Chung Y H. Effect of turbulence and noise on ultraviolet and mid-infrared spectrum in optical wireless communications. Photon Netw Commun, 2020, 39: 181–186
5 Cheng Z M, Shuai Y, Gong D Y, et al. Optical properties and cooling performance analyses of single-layer radiative cooling coating with mixture of TiO_2 particles and SiO_2 particles. Sci China Tech Sci, 2021, 64: 1017–1029
6 Song Q, Zhou Y, Jia E S, et al. Large area crystalline Weyl semimetal with nano Au film based micro-fold line array for THz detector. Sci China Tech Sci, 2023, 66: 3267–3275
7 Xue X W, Calabretta N. Nanosecond optical switching and control system for data center networks. Nat Commun, 2022, 13: 2257
8 Liu Z H, Li X, Zhang Y, et al. Fiber end-facet integrated non-volatile optical switch based on $Ge_2Sb_2Te_5$. J Lightwave Technol, 2022, 40: 3968–3973
9 Konoike R, Suzuki K, Kawashima H, et al. Port-alternated switch-and-select optical switches. J Lightwave Technol, 2021, 39: 1102–1107
10 Guo Y M, Xiong B, Shuai Y, et al. Thermal driven wavelength-selective optical switch based on magnetic polaritons coupling. J Quant Spectrosc Ra, 2020, 255: 107230
11 Wang Q, Zhang S J, Wang C, et al. Tunable infrared optical switch based on vanadium dioxide. Nanomaterials, 2021, 11: 2988
12 Saitzek S, Guirleo G, Guinneton F, et al. New thermochromic bilayers for optical or electronic switching systems. Thin Solid Films, 2004, 449: 166–172
13 Dehghan M, Moravvej-Farshi M K, Jabbari M, et al. Bistable terahertz switch designed by integration of a graphene plasmonic crystal into Fabry-Perot resonator. IEEE J Sel Top Quantum Electron, 2021, 27: 1–6
14 Chen S, Yi X, Ma H, et al. A novel structural VO_2 micro-optical switch. Optical Quantum Electron, 2003, 35: 1351–1355
15 Daniel S, Saastamoinen K, Saastamoinen T, et al. Dynamic control of optical transmission through a nano-slit using surface plasmons. Opt Express, 2015, 23: 22512–22519
16 Wan M L, Zhai W Q, Song Y L, et al. Actively controllable EIT-like resonance between localized and propagating surface plasmons for optical switching. J Modern Opt, 2015, 62: 1264–1269
17 Guo Y M, Zhu L W, Chen S N, et al. Dual-band polarized optical switch with opposite thermochromic properties to vanadium dioxide. Appl Phys Lett, 2022, 121: 201102
18 Sámson Z L, MacDonald K F, De Angelis F, et al. Metamaterial electro-optic switch of nanoscale thickness. Appl Phys Lett, 2010, 96: 143105
19 Araki K, Zhang R Z. Infrared radiative switching with thermally and electrically tunable transition metal oxides-based plasmonic grating. Sci Rep, 2023, 13: 3702
20 Li Z Q, Chen W. Progress in dynamic emissivity regulation: Control methods, material systems, and applications. Mater Chem Front, 2021, 5: 6315–6332
21 Barker A S, Verleur H W, Guggenheim H J. Infrared optical properties of vanadium dioxide above and below the transition temperature. Phys Rev Lett, 1966, 17: 1286–1289
22 Chu C H, Tseng M L, Chen J, et al. Active dielectric metasurface based on phase-change medium. Laser Photonics Rev, 2016, 10: 986–994
23 Semenov A L. Time of a semiconductor-metal phase transition induced by an ultrashort light pulse in vanadium dioxide. Phys Solid State, 2007, 49: 1157–1160
24 Miller K J, Haglund R F, Weiss S M. Optical phase change materials in integrated silicon photonic devices: Review. Opt Mater Express, 2018, 8: 2415–2429
25 Outón J, Casas-Acuña A, Domínguez M, et al. Novel laser texturing of W-doped VO_2 thin film for the improvement of luminous transmittance in smart windows application. Appl Surf Sci, 2023, 608: 155180
26 Mai L Q, Hu B, Hu T, et al. Electrical property of Mo-doped VO_2 nanowire array film by melting-quenching sol-gel method. J Phys Chem B, 2006, 110: 19083–19086
27 Qin S Z, Fan Y C, Qiu X, et al. Modulation of the phase transition behavior of VO_2 nanofilms by the coupling of Zr doping and size-dependent band gap. SSRN J, 2022, 4: 6067
28 Xie Z T, Wu J Y, Fu H Y, et al. Tunable electro- and all-optical switch based on epsilon-near-zero metasurface. IEEE Photonics J, 2020, 12: 1–10
29 Dalal K, Sharma Y. Broadband plasmonic switches based on nano-disc-dimers with progressively increasing diameters on a plasmonic film with a VO_2 spacer. Optics Commun, 2023, 530: 129121
30 Markov P, Appavoo K, Haglund R F, et al. Hybrid Si-VO_2-Au optical

modulator based on near-field plasmonic coupling. Opt Express, 2015, 23: 6878–6887
31 Thomas A, Savaliya P, Kumar K, et al. Au nanowire-VO_2 spacer-Au film based optical switches. J Opt Soc Am B, 2018, 35: 1687–1697
32 Wen S, Zhang Y H, Ma Y C, et al. Dirac semimetal-assisted near-field radiative thermal rectifier and thermostat based on phase transition of vanadium dioxide. Opt Express, 2023, 31: 34362–34380
33 Qu Y R, Cai L, Luo H, et al. Tunable dual-band thermal emitter consisting of single-sized phase-changing GST nanodisks. Opt Express, 2018, 26: 4279–4287
34 Zeng B, Huang Z, Singh A, et al. Hybrid graphene metasurfaces for high-speed mid-infrared light modulation and single-pixel imaging. Light Sci Appl, 2018, 7: 51
35 Zhang X P, Cheng Z M, Yang D L, et al. Scalable bio-skin-inspired radiative cooling metafabric for breaking trade-off between optical properties and application requirements. ACS Photon, 2023, 10: 1624–1632
36 Dong Y, Meng W F, Wang F Q, et al. "Warm in winter and cool in summer": Scalable biochameleon inspired temperature-adaptive coating with easy preparation and construction. Nano Lett, 2023, 23: 9034–9041
37 Hong Y, Ma Y C, Wen S, et al. A reconstructed approach for online prediction of transient heat flux and interior temperature distribution in thermal protect system. Int Commun Heat Mass Transfer, 2023, 148: 107055
38 Guo Y M, Pang S J, Luo Z J, et al. Measurement of directional spectral emissivity at high temperatures. Int J Thermophys, 2019, 40: 10
39 Cai W S, White J S, Brongersma M L. Compact, high-speed and power-efficient electrooptic plasmonic modulators. Nano Lett, 2009, 9: 4403–4411
40 Khoshman J M, Kordesch M E. Optical properties of a-HfO_2 thin films. Surf Coat Tech, 2006, 201: 3530–3535
41 Wang L P, Zhang Z M. Resonance transmission or absorption in deep gratings explained by magnetic polaritons. Appl Phys Lett, 2009, 95: 111904
42 Guo Y M, Shuai Y, Zhao J M. Tailoring radiative properties with magnetic polaritons in deep gratings and slit arrays based on structural transformation. J Quant Spectrosc Ra, 2020, 242: 106788
43 Guo Y M, Shuai Y, Tan H P. Mechanism of polaritons coupling from perspective of equivalent MLC circuits model in slit arrays. Opt Express, 2019, 27: 21173–21184
44 Lee B J, Wang L P, Zhang Z M. Coherent thermal emission by excitation of magnetic polaritons between periodic strips and a metallic film. Opt Express, 2008, 16: 11328–11336
45 Yang P Y, Ye H, Zhang Z M M. Experimental demonstration of the effect of magnetic polaritons on the radiative properties of deep aluminum gratings. J Heat Transfer, 2019, 141: 052702
46 Cai Y P, Huang Y, Zhu K Y, et al. Direction-independent dual-band perfect absorption induced by fundamental magnetic polaritons. Opt Express, 2019, 27: A1431
47 Kim K D, Han D N, Kim H T. Optimization of experimental conditions based on the Taguchi robust design for the formation of nano-sized silver particles by chemical reduction method. Chem Eng J, 2004, 104: 55–61
48 Choi J, Kim M, Kang K, et al. Robust optimization of a tandem grating solar thermal absorber. J Quant Spectrosc Ra, 2018, 209: 129–136
49 Volz F E. Depth and shape of the 94-μm water vapor absorption band for clear and cloudy skies. Appl Opt, 1969, 8: 2261–2264
50 Liu D D, Huang Y B, Sun Y S, et al. Observation of greenhouse gases and their impacts on atmospheric transmittance. In: Proceedings of the 14th National Conference on Laser Technology and Optoelectronics (LTO), SPIE (Spie-Int Soc Optical Engineering). Shanghai, 2019
51 Tkacik D S, Luna-Cruz Y, Clinton N, et al. Atmospheric correction for MASTER image data using localized modelled and observed meteorology and trace gases. Remote Sens Lett, 2012, 3: 201–209